

1 **Sensitivity of airborne geophysical data to sublacustrine**  
2 **and near-surface permafrost thaw**

3

4 **Burke J. Minsley<sup>1</sup>, Tristan P. Wellman<sup>2</sup>, Michelle A. Walvoord<sup>3</sup>, and André**  
5 **Revil<sup>4,5</sup>**

6

7 [1] {U.S. Geological Survey, Crustal Geophysics and Geochemistry Science Center,  
8 Denver, Colorado}

9 [2] {U.S. Geological Survey, Colorado Water Science Center, Denver, Colorado}

10 [3] {U.S. Geological Survey, National Research Program, Denver, Colorado}

11 [4] {Colorado School of Mines, Department of Geophysics, Golden, Colorado}

12 [5] {JSTerre, CNRS, UMR CNRS 5275, Université de Savoie, Le Bourget du Lac,  
13 France}

14

15

16

17

18

19

20 **Abstract**

21 A coupled hydrogeophysical forward and inverse modeling approach is developed to  
22 illustrate the ability of frequency-domain airborne electromagnetic (AEM) data to  
23 characterize subsurface physical properties associated with sublacustrine permafrost thaw  
24 during lake talik formation. Numerical modeling scenarios are evaluated that consider  
25 non-isothermal hydrologic responses to variable forcing from different lake depths and  
26 for different hydrologic gradients. A novel physical property relationship connects the  
27 dynamic distribution of electrical resistivity to ice-saturation and temperature outputs  
28 from the SUTRA groundwater simulator with freeze/thaw physics. The influence of  
29 lithology on electrical resistivity is controlled by a surface conduction term in the  
30 physical property relationship. Resistivity models, which reflect changes in subsurface  
31 conditions, are used as inputs to simulate AEM data in order to explore the sensitivity of  
32 geophysical observations to permafrost thaw. Simulations of sublacustrine talik  
33 formation over a 1,000-year period are modeled after conditions found in the Yukon  
34 Flats, Alaska. Synthetic AEM data are analyzed with a Bayesian Markov chain Monte  
35 Carlo algorithm that quantifies geophysical parameter uncertainty and resolution. Major  
36 lithological and permafrost features are well resolved by AEM data in the examples  
37 considered. The subtle geometry of partial ice-saturation beneath lakes during talik  
38 formation cannot be resolved using AEM data, but the gross characteristics of sub-lake  
39 resistivity models reflect bulk changes in ice content and can identify the presence of a  
40 talik. A final synthetic example compares AEM and ground-based electromagnetic  
41 responses for their ability to resolve shallow permafrost and thaw features in the upper 1-  
42 2 m below ground outside the lake margin.

43

## 44 **1 Introduction**

45 Permafrost thaw can have important consequences for the distribution of surface water  
46 (Roach et al., 2011; Rover et al., 2012), stream discharge and chemistry (O'Donnell et  
47 al., 2012; Petrone et al., 2007; Striegl et al., 2005; Walvoord and Striegl, 2007), and  
48 exchange between groundwater and surface water systems (Bense et al., 2009; Callegary  
49 et al., 2013; Walvoord et al., 2012). Likewise, hydrologic changes that alter the thermal  
50 forcing supplied by surface water or groundwater systems can modify the distribution of  
51 permafrost, illustrating the strong feedbacks between permafrost and hydrology. In  
52 addition to hydrologic processes, permafrost is affected by climate warming in Arctic and  
53 sub-Arctic regions (Hinzman et al., 2005; Jorgenson et al., 2001), as well as disturbance  
54 by fire (Yoshikawa et al., 2002). Climate feedbacks associated with permafrost thaw  
55 include changes in the amount of organic carbon stored in soils that is vulnerable to  
56 decomposition (Koven et al., 2011; O'Donnell et al., 2011) and subsequent methane and  
57 carbon dioxide released from soils by the degradation of organic material previously  
58 sequestered in frozen ground (Anthony et al., 2012). Permafrost thaw also has significant  
59 implications for land management and infrastructure, including the potential to damage  
60 buildings, roadways, or pipelines due to ground settling, and thermal erosion that can  
61 alter coastlines and landscape stability (Larsen et al., 2008; Nelson et al., 2002).

62 Several investigations have shown the significance of climate and advective heat  
63 transport in controlling the distribution of permafrost in hydrologic systems (Bense et al.,  
64 2009; Rowland et al., 2011; Wellman et al., 2013). These results yield important insight  
65 into the mechanistic behavior of coupled thermal-hydrologic systems, and are a means  
66 for predicting the impact on permafrost from a wide range of climate and hydrologic  
67 conditions. However, few techniques are capable of assessing the distribution of  
68 permafrost, and most approaches only capture a single snapshot in time.

69 Satellite remote-sensing techniques have proven useful in detecting the distribution and  
70 changes in shallow permafrost, vegetation, and active layer thickness over large areas  
71 (Liu et al., 2012; Panda et al., 2010; Pastick et al., 2014), but are only sensitive to very  
72 near-surface properties. Borehole cores and downhole temperature or geophysical logs  
73 provide direct information about permafrost and geologic structures, but tend to be

74 sparsely located and are not always feasible in remote areas. Geophysical methods are  
75 necessary for investigating subsurface physical properties over large and/or remote areas.  
76 Recent examples of geophysical surveys aimed at characterizing permafrost in Alaska  
77 include: an airborne electromagnetic (AEM) survey used to delineate geologic and  
78 permafrost distributions in an area of discontinuous permafrost (Minsley et al., 2012a),  
79 ground-based electrical measurements used to assess shallow permafrost aggradation  
80 near recently receded lakes (Briggs et al., 2014), electrical and electromagnetic surveys  
81 used to characterize shallow active layer thickness and subsurface salinity (Hubbard et  
82 al., 2013), and surface nuclear magnetic resonance (sNMR) soundings used to infer the  
83 thickness of unfrozen sediments beneath lakes (Parsekian et al., 2013). A challenge with  
84 geophysical methods, however, is that geophysical properties (e.g. electrical resistivity)  
85 are only indirectly sensitive to physical properties of interest (e.g. lithology, water  
86 content, thermal state). In addition, various physical properties can produce similar  
87 electrical resistivity values. Therefore, it is critically important to understand the  
88 relationship between geophysical properties and the ultimate physical properties and  
89 processes of interest (Minsley et al., 2011; Rinaldi et al., 2011).

90 The non-isothermal hydrologic simulations of Wellman et al. (2013) predict the evolution  
91 of lake taliks (unfrozen sub-lacustrine areas in permafrost regions) in a two-dimensional  
92 axis-symmetric model under different environmental scenarios (e.g. lake size, climate,  
93 groundwater flow regime). Here, we investigate the ability of geophysical measurements  
94 to recover information about the underlying spatial distribution of permafrost and  
95 hydrologic properties. This is accomplished in three steps: (1) development of a physical  
96 property relation that connects permafrost and hydrologic properties to geophysical  
97 properties; (2) generation of synthetic geophysical data that would be expected for  
98 various permafrost hydrologic conditions that occur during simulated lake talik  
99 formation; and (3) inversion of the synthetic geophysical data using realistic levels of  
100 noise to investigate the ability to resolve specific physical features of interest. Our focus  
101 is on electromagnetic geophysical methods as these types of data have previously been  
102 acquired near Twelvemile Lake in the Yukon Flats, Alaska (Ball et al., 2011; Minsley et  
103 al., 2012a); a lake that is also the basis for the lake simulations discussed by Wellman et  
104 al. (2013).

## 105 **2 Methods**

### 106 **2.1 Coupled Thermal-hydrologic Simulations**

107 Wellman et al. (2013) describe numerical simulations of lake-talik formation in  
108 watersheds modeled after those found in the lake-rich Yukon Flats of interior Alaska.  
109 Modeling experiments used the SUTRA groundwater modeling code (Voss and Provost,  
110 2002) enhanced with capabilities to simulate freeze-thaw processes (McKenzie and Voss,  
111 2013). The phase change between ice and liquid water occurs over a specified  
112 temperature range, and accounts for latent heat of fusion as well as changes in thermal  
113 conductivity and heat capacity for ice-water mixtures. Ice content also changes the  
114 effective permeability, thereby altering subsurface flowpaths and enforcing a strong  
115 coupling between hydraulic and thermal processes. The modeling domain, which is  
116 adapted for this study, is axis-symmetric with a central lake and upwards-sloping ground  
117 surface that rises from an elevation of 500 m at  $r = 0$  m to 520 m at the outer extent of the  
118 model,  $r = 1800$  m (Figure 1). The model uses a layered-geology consistent with the  
119 Yukon Flats (Minsley et al., 2012a; Williams, 1962), with defined hydrologic and  
120 geophysical parameters for each layer summarized in Table 1. Initial permafrost  
121 conditions prior to lake formation were established by running the model to steady state  
122 under hydrostatic conditions with a constant temperature of  $-2.25$  °C applied to the land  
123 surface, which produces a laterally continuous permafrost layer extending to a depth of  
124 about 90 m.

125 Subsequent hydrologic simulations assume fully saturated conditions, and are performed  
126 over a 1,000-year period under 36 different scenarios of climate (warmer than, colder  
127 than, and similar-to present conditions); hydrologic gradient (hydrostatic, gaining, and  
128 losing lake conditions); and lake depth/extent (3-, 6-, 9-, and 12-m-deep lakes that  
129 intersect the ground surface at increasing distance, as shown in Figure 1). Complete  
130 details and results of the hydrologic simulations can be found in Wellman et al. (2013).  
131 At each simulation time step, the SUTRA model outputs temperature, pressure, and ice  
132 saturation. Conversion of these hydrologic variables to electrical resistivity- the  
133 geophysical property needed to simulate electromagnetic data considered here- is  
134 described below.

## 135 2.2 A physical property relationship

136 Electrical resistivity is the primary geophysical property of interest for the  
137 electromagnetic geophysical methods used in this study. It is well-established that  
138 resistivity is sensitive to basic physical properties such as unfrozen water content, soil or  
139 rock texture, and salinity (Palacky, 1987). Here, we build on earlier efforts to simulate  
140 the electrical properties of ice-saturated media (Hauck et al., 2011) by using a modified  
141 form of Archie's Law (Archie, 1942) that also incorporates surface conduction effects  
142 (Revil, 2012) to predict the dynamic electrical resistivity structure for the evolving state  
143 of temperature and ice saturation ( $S_i$ ) in the talik simulations. Bulk electrical  
144 conductivity is described by *Revil* (2012) as

$$145 \quad \sigma = \frac{S_w^n}{F} \left[ \sigma_f + m(S_w^{-n} F - 1) \sigma_s \right], \quad (1)$$

146 where  $\sigma$  is the bulk electrical conductivity [S/m];  $S_w$  is the fractional water saturation [-]  
147 in the pore space, where  $S_w = 1 - S_i$ ;  $\sigma_f$  is the conductivity of the saturating pore fluid  
148 [S/m];  $m$  is the Archie cementation exponent [-];  $n$  is the Archie saturation exponent [-];  
149  $F$  is the formation factor [-], where  $F = \phi^{-m}$  and  $\phi$  is the matrix porosity [-]; and  $\sigma_s$  is the  
150 conductivity [S/m] associated with grain surfaces. The Archie exponents  $m$  and  $n$  are  
151 known to vary as a function of pore geometry; here, we use  $m = n = 1.5$ , which is  
152 appropriate for unconsolidated sediments (Sen et al., 1981). Simulation results are  
153 presented as electrical resistivity [ohm-m], which is the inverse of the conductivity, i.e.  $\rho$   
154  $= 1/\sigma$ .

155 The first term in Eq. (1) describes electrical conduction within the pore fluid, where fluid  
156 conductivity is defined as

$$157 \quad \sigma_f = F_c \sum_i \beta_i |z_i| C_i . \quad (2)$$

158 The summation in Eq. (2) is over all dissolved ionic species ( $\text{Na}^+$  and  $\text{Cl}^-$  are assumed to  
159 be the primary constituents in this study), where  $F_c$  is Faraday's constant [C/mol] and  $C_i$ ,  
160  $\beta_i$ , and  $z_i$  are the concentration [mol/L], ionic mobility [ $\text{m}^2/\text{Vs}$ ], and valence of the  $i^{\text{th}}$   
161 species, respectively.

162 Surface conduction effects, described by the second term in Eq. (1), are related to the  
 163 chemistry at the pore-water interface, and can be important in fresh water (low  
 164 conductivity) systems at low porosity (high ice saturation). Additionally, the surface  
 165 conduction term provides a means for describing the conductivity behavior for different  
 166 lithologies, as will be described below. The surface conductivity is given by

$$167 \quad \sigma_s = \frac{2}{3} \left( \frac{\phi}{1-\phi} \right) \beta_s Q_v, \quad (3)$$

168 where  $\beta_s$  is the cation mobility [ $\text{m}^2/\text{Vs}$ ] for counterions in the electrical double layer at the  
 169 grain-water interface (Revil et al., 1998) and  $Q_v$  is the excess electrical charge density  
 170 [ $\text{C}/\text{m}^3$ ] in the pore volume,

$$171 \quad Q_v = S_w^{-1} \rho_g \left( \frac{1-\phi}{\phi} \right) \chi, \quad (4)$$

172 where  $\rho_g$  is the mass density of the grains [ $\text{kg}/\text{m}^3$ ] and  $\chi$  is the cation exchange capacity  
 173 [ $\text{C}/\text{kg}$ ]. Changes in  $\chi$ , representative of bulk differences in clay mineral content, are used  
 174 to differentiate the electrical signatures of the lithologic units in this study (Table 1).

175 The temperature,  $T$  [C], dependence of ionic mobility affects both the fluid conductivity  
 176 (Eq. (2)) and surface conductivity (Eq. (3)), where mobility is approximated as a linear  
 177 function of temperature (Keller and Frischknecht, 1966; Sen and Goode, 1992) as

$$178 \quad \beta(T) = \beta_{T=25\text{C}} [1 + 0.019(T - 25)]. \quad (5)$$

179 Finally, we consider the effect of increasing ice saturation on salinity. Because salts are  
 180 generally excluded as freezing occurs, salinity of the remaining unfrozen pore water is  
 181 expected to increase with increasing ice content (Marion, 1995), leading to a  
 182 corresponding increase in fluid conductivity according to Eq. (2). To describe this  
 183 dependence of salinity on ice saturation,  $C(S_i)$ , we use the expression

$$184 \quad C(S_i) = C_{S_i=0} S_w^{-\alpha}, \quad (6)$$

185 where  $\alpha \sim 0.8$  accounts for loss of solute from the pore space due to diffusion or other  
 186 transport processes, and  $S_i = 1 - S_w$ .

187 Information about the different lithologic units described by Wellman et al. (2013) that  
188 are also summarized in Table 1 are used to define static model properties such as  
189 porosity, grain mass density, cation exchange capacity, and Archie's exponents.  
190 Dynamic outputs from the SUTRA simulations, including temperature and ice saturation,  
191 are combined with the static variables in Eqs. (1) - (6) to predict the evolving electrical  
192 resistivity structure.

### 193 **2.3 Geophysical Forward Simulations**

194 Synthetic airborne electromagnetic (AEM) data are simulated for each snapshot of  
195 predicted bulk resistivity values using nominal system parameters based on the Fugro  
196 RESOLVE<sup>1</sup> frequency-domain AEM system that was used in the Yukon Flats survey  
197 (Minsley et al., 2012a). The RESOLVE system consists of five horizontal coplanar  
198 (HCP) transmitter-receiver coil pairs separated by approximately 7.9 m that operate at  
199 frequencies 0.378 kHz, 1.843 kHz, 8.180 kHz, 40.650 kHz, and 128.510 kHz; and one  
200 vertical coaxial (VCX) coil pair with 9-m separation that operates at 3.260 kHz.

201 Oscillating currents and associated magnetic fields created by the transmitter coils induce  
202 electrical currents in the subsurface that, in turn, generate secondary magnetic fields that  
203 are recorded by the receiver coils (Siemon, 2006; Ward and Hohmann, 1988). Data are  
204 reported as in-phase and quadrature components of the secondary field in parts-per-  
205 million (ppm) of the primary field, and responses as a function of frequency can be  
206 converted through mathematical inversion to estimates of electrical resistivity as a  
207 function of depth (e.g., Farquharson et al., 2003). Data are simulated at the nominal  
208 survey elevation of 30 m above ground surface using the one-dimensional modeling  
209 algorithm described in Minsley (2011), which follows the standard electromagnetic  
210 theory presented by Ward and Hohmann (1988).

211 The vertical profile of resistivity as a function of depth is extracted at each survey  
212 location and is used to simulate forward geophysical responses. There are 181 sounding  
213 locations for each axis-symmetric model, starting at the center of the lake ( $r = 0$  m) to the  
214 edge of the model domain ( $r = 1,800$  m) in 10-m increments. Each vertical resistivity

---

<sup>1</sup> Any use of trade, product, or firm names is for descriptive purposes only and does not imply endorsement by the U.S. Government

215 profile extends to 200 m depth, which is well beyond the depth to which we expect to  
216 recover parameters in the geophysical inversion step. A center-weighted 5-point filter  
217 with weights equal to [0.0625, 0.25, 0.375, 0.25, 0.0625] is used to average neighboring  
218 bulk resistivity values at each depth before modeling in order to partly account for the  
219 lateral sensitivity of AEM systems (Beamish, 2003). Forward simulations are repeated  
220 for each of the 50 simulation times between 0 and 1,000 years output from SUTRA,  
221 resulting in 9,050 data locations per modeling scenario.

222 Synthetic ground-based electromagnetic data presented in Section 3.3 are simulated using  
223 nominal system parameters based on the GEM-2 instrument (Huang and Won, 2003).  
224 The GEM-2 has a single HCP transmitter-receiver pair separated by 1.66 m, and data are  
225 simulated at six frequencies: 1.5 kHz, 3.5 kHz, 8.1 kHz, 19 kHz, 43 kHz, and 100 kHz.  
226 A system elevation of 1 m above ground is assumed, which is typical for this hand-  
227 carried instrument.

## 228 **2.4 Parameter Estimation and Uncertainty Quantification**

229 The inverse problem involves estimating subsurface resistivity values given the simulated  
230 forward responses and realistic assumptions about data errors. Geophysical inversion is  
231 inherently uncertain; there are many plausible resistivity models that are consistent with  
232 the measured data. In addition, the ability to resolve true resistivity values is limited both  
233 by the physics of the AEM method and the level of noise in the data. Here, we use a  
234 Bayesian Markov chain Monte Carlo (McMC) algorithm developed for frequency-  
235 domain EM data (Minsley, 2011) to explore the ability of simulated AEM data to recover  
236 the true distribution of subsurface resistivity values at 20-year intervals within the 1,000-  
237 year lake talik simulations. This McMC approach is an alternative to traditional  
238 inversion methods that find a single ‘optimal’ model that minimizes a combined measure  
239 of data fit and model regularization (Aster et al., 2005). Although computationally more  
240 demanding, McMC methods allow for comprehensive model appraisal and uncertainty  
241 quantification. AEM-derived resistivity estimates for the simulations considered here  
242 will help guide interpretations of future field datasets, identifying the characteristics of  
243 relatively young versus established thaw under different hydrologic conditions.

244 The MCMC algorithm provides comprehensive model assessment and uncertainty  
245 analysis, and is useful in diagnosing the ability to resolve various features of interest. At  
246 every data location along the survey profile, an ensemble of 100,000 resistivity models is  
247 generated according to the Metropolis-Hastings algorithm (Hastings, 1970; Metropolis et  
248 al., 1953). According to Bayes' theorem, each model is assigned a posterior probability  
249 that is a measure of (1) its prior probability which, in this case, is used to penalize models  
250 with unrealistically large contrasts in resistivity over thin layers; and (2) its data  
251 likelihood, which is a measure of how well the predicted data for a given resistivity  
252 model match the observed data within data errors. A unique aspect of this algorithm is  
253 that it does not presuppose the number of layers needed to fit the observed data, which  
254 helps avoid biases due to assumptions about model parameterization. Instead, trans-  
255 dimensional sampling rules (Green, 1995; Sambridge et al., 2013) are used to allow the  
256 number of unknown layers to be one of the unknowns. That is, the unknown parameters  
257 for each model include the number of layers, layer interface depths, and resistivity values  
258 for each layer.

259 Numerous measures and statistics are generated from the ensemble of plausible resistivity  
260 models, such as: the single most-probable model, the probability distribution of resistivity  
261 values at any depth, the probability distribution of where layer interfaces occur as a  
262 function of depth, and the probability distribution of the number of layers (model  
263 complexity) needed to fit the measured data. A detailed description of the MCMC  
264 algorithm can be found in Minsley (2011). Finally, probability distributions of resistivity  
265 are combined with assumptions about the distribution of resistivity values for any  
266 lithology and/or ice content in order to make a probabilistic assessment of lithology or ice  
267 content, as illustrated below.

## 268 **3 Results**

### 269 **3.1 Electrical resistivity model development**

270 Information about the different lithologic units described by Wellman et al. (2013) that  
271 are also summarized in Table 1 are used to define static model properties such as  
272 porosity, grain mass density, cation exchange capacity, and Archie's exponents.  
273 Dynamic outputs from the SUTRA simulations, including temperature and ice saturation,

274 are combined with the static variables in Eqs. (1) - (6) to predict the evolving electrical  
275 resistivity structure. The behavior of bulk resistivity as a function of ice saturation is  
276 shown in Figure 2. Separate curves are shown for a range of  $\chi$  (cation exchange capacity)  
277 values, which are the primary control in defining offset resistivity curves for different  
278 lithologies, where increasing  $\chi$  is generally associated with more fine-grained material  
279 such as silt or clay.

280 For each of the 1,000-year simulations, the static variables summarized in Table 1 are  
281 combined with the spatially and temporally variable state variables  $T$  and  $S_i$  output by  
282 SUTRA to predict the distribution of bulk resistivity at each time step using Eqs. (1) - (6).  
283 An example of SUTRA output variables for the 6 m-deep gaining lake scenario at 240  
284 years (the approximate sub-lake talik breakthrough time for that scenario) is shown in  
285 Figure 3A-B, and the predicted resistivity for this simulation step is shown in Figure 3C.  
286 The influence of different lithologic units is clearly manifested in the predicted resistivity  
287 values, whereas lithology is not overly evident in the SUTRA state variables. For a  
288 single unit, there is a clear difference in resistivity for frozen versus unfrozen conditions.  
289 Across different units, there is a contrast in resistivity when both units are frozen or  
290 unfrozen. Resistivity can therefore be a valuable indicator of both geologic and ice  
291 content variability. However, there is also ambiguity in resistivity values as both  
292 unfrozen Unit 2 and frozen Unit 3 appear to have intermediate resistivity values of  
293 approximately 100-300 ohm-m (Figure 3C) and cannot be characterized by their  
294 resistivity values alone. This ambiguity in resistivity can only be overcome by additional  
295 information such as borehole data or prior knowledge of geologic structure. Synthetic  
296 bulk resistivity values according to Eq. (1) are shown in Figure 4 for the four different  
297 lake depths (3, 6, 9, and 12 m) at three different simulation times (100, 240, and 1,000  
298 years) output from the hydrostatic/current climate condition simulations.

299 Lithology and ice saturation are the primary factors that control simulated resistivity  
300 values (Figure 2), though ice saturation is a function of temperature. The empirical  
301 relation between temperature and bulk resistivity is shown in Figure 3D by cross-plotting  
302 values from Figure 3B-C. Within each lithology resistivity is relatively constant above  
303 zero degrees, with a rapid increase in resistivity for temperatures below zero degrees.  
304 This result is very similar to the temperature-resistivity relationships illustrated by

305 Hoekstra (1975, Fig. 1), lending confidence to our physical property definitions described  
306 earlier. Above zero degrees, the slight decrease in resistivity is due to the temperature-  
307 dependence of fluid resistivity. The rapid increase in resistivity below zero degrees is  
308 primarily caused by reductions in effective porosity due to increasing ice saturation,  
309 though changes in surface conductivity and salinity at increasing ice saturation are also  
310 contributing factors. Below -1C, the change in resistivity values as a function of  
311 temperature rapidly decreases. This is an artifact caused by the imposed temperature-ice  
312 saturation relationship defined in SUTRA that, for these examples, enforces 99% ice  
313 saturation at -1C. It is more likely that ice saturation continues to increase asymptotically  
314 over a larger range of temperatures below zero degrees, with corresponding increases in  
315 electrical resistivity. However, because AEM methods are limited in their ability to  
316 discern differences among very high resistivity values, as discussed later, this artifact  
317 does not significantly impact the results presented here.

### 318 **3.2 Parameter Estimation and Uncertainty Quantification**

319 AEM data (not shown) are simulated for each of the electrical resistivity models (e.g.  
320 Figure 4) using the methods described in Section 2.3. The simulated data are then used to  
321 recover estimates of the original resistivity values according to the approach outlined in  
322 Section 2.4, assuming 4% data error with an absolute error floor of 5 ppm. Resistivity  
323 parameter estimation results for the 6 m-deep hydrostatic lake scenario (Figure 4, D-F)  
324 are shown in Figure 5. At each location along the profile, the average resistivity model as  
325 a function of depth is calculated from the MCMC ensemble of 100,000 plausible models.  
326 The overall pattern of different lithologic units and frozen/unfrozen regions is accurately  
327 depicted in Figure 5, with two exceptions that will be discussed in greater detail: (1) the  
328 specific distribution of partial ice saturation beneath the lake before thaw has equilibrated  
329 (Figure 5A-B); and (2) the shallow sand layer (Unit 1) that is generally too thin to be  
330 resolved using AEM data.

331 A point-by-point comparison of true (Figure 4F) versus predicted (Figure 5C) resistivity  
332 values for the hydrostatic 6 m-deep lake scenario at the simulation time 1,000 years is  
333 shown in Figure 6A. The cross-plot of true versus estimated resistivity values generally  
334 fall along the 1:1 line, providing a more quantitative indication of the ability to estimate

335 the subsurface resistivity structure. Estimates of the true resistivity values for each  
336 lithology and freeze/thaw state (Figure 6B) tend to be indistinct; appearing as a vertical  
337 range of possible values in Figure 6A due to the inherent resolution limitations of inverse  
338 methods and parameter tradeoffs (Day-Lewis, F. D. et al., 2005; Oldenborger and Routh,  
339 2009). Although the greatest point density for both frozen and unfrozen silts (Unit 3)  
340 falls along the 1:1 line, resistivity values for these components of the model are also often  
341 overestimated; this is likely due to uncertainties in the location of the interface between  
342 the silt and gravel units. This is in contrast with the systematic underestimation of frozen  
343 gravel resistivity values due to the inability to discriminate very high resistivity values  
344 using EM methods (Ward and Hohmann, 1988). Frozen sands (true log resistivity  $\sim 2.8$   
345 in Figure 6B) are also systematically overestimated in Figure 6A; in this case, due to the  
346 inability to resolve this relatively thin resistive layer.

347 While useful, single ‘best’ estimates of resistivity values at any location (Figure 6) are  
348 not fully representative of the information contained in the AEM data and associated  
349 model uncertainty. From the MCMC analysis of 100,000 models at each data location,  
350 estimates of the posterior probability density function (pdf) of resistivity are generated for  
351 each point in the model. Probability distributions are extracted from a depth of 15 m,  
352 within the gravel layer (Unit 2), at one location where unfrozen conditions exist ( $r = 0$   
353 m), and a second location outside the lake extent ( $r = 750$  m) where the ground remains  
354 frozen (Figure 7A). Results from a depth of 50 m, within the silt layer (Unit 3), are  
355 shown in Figure 7B. With the exception of the frozen gravels, whose resistivity tends to  
356 be underestimated, the peak of each pdf is a good estimate of the true resistivity value at  
357 that location.

358 Resistivity values are translated to estimates of ice saturation, which is displayed on the  
359 upper axis of each panel in Figure 7, using the appropriate lithology curve from Figure 2.  
360 Using the ice saturation-transformed pdfs, quantitative inferences can be made about the  
361 probability of the presence or absence of permafrost. For example, the probability of ice  
362 content being less than 50% is estimated by calculating the fractional area under each  
363 distribution for ice-content values less than 0.5. Probability estimates of ice content less  
364 than 50% and greater than 95% for the four distributions shown in Figure 7 are  
365 summarized in Table 2. High probabilities of ice content exceeding 95% are associated

366 with the  $r = 750$  m location outside the lake extent, whereas high probability of ice  
367 content below the 50% threshold are observed at  $r = 0$  beneath the center of the lake. The  
368 pdfs for each lithology shown in Figure 7 are end-member examples of frozen and  
369 unfrozen conditions. Within a given lithology, a smooth transition from the frozen-state  
370 pdf to the unfrozen-state pdf is observed as thaw occurs, with corresponding transitions in  
371 the calculated ice threshold probabilities.

372 Further illustration of the spatial and temporal changes in resistivity pdfs are shown in  
373 Figure 8. The resistivity pdf is displayed as a function of distance from the lake center at  
374 the same depths (15 m and 50 m) shown in Figure 7, corresponding to gravel (Figure  
375 8A,C, and E) and silt (Figure 8B, D, and F) locations. High probabilities, i.e. the peaks in  
376 Figure 7, correspond to dark-shaded areas in Figure 8. Images are shown for three  
377 different time steps in the SUTRA simulation for the hydrostatic 6 m-deep lake scenario:  
378 100 years (Figure 8A-B), 240 years (Figure 8C-D), and 1,000 years (Figure 8E-F).  
379 Approximate ice-saturation values, translated from the ice versus resistivity relationships  
380 for each lithology shown in Figure 2, are displayed on the right axis of each panel in  
381 Figure 8, and true resistivity values are plotted as a dashed line. Observations from  
382 Figure 8 include:

383 (1) Outside the lake boundary, pdfs are significantly more sharply peaked (darker  
384 shading) for the gravel unit than the silt unit, suggesting better resolution of shallower  
385 resistivity values within the gravel layer. It should be noted however, that this improved  
386 resolution does not imply improved model accuracy; in fact, the highest probability  
387 region slightly underestimates the true resistivity value. (2) Probability distributions for  
388 the silt layer track the true values, but with greater uncertainty. (3) Inside the lake  
389 boundary, gravel resistivity values are not as well resolved compared with locations  
390 outside the lake boundary due to the loss of signal associated with the relatively  
391 conductive lake water. (4) Increasing trends in resistivity/ice saturation towards the outer  
392 extents of the lake are captured in the pdfs, but are subtle. (5) Within the silt layer at  
393 early times before the talik is fully through-going (Figure 8B, D), the AEM data are  
394 insensitive to which layer is present, hence the bi-modal resistivity distribution with  
395 peaks associated with characteristic silt and gravel values. This ambiguity disappears at

396 later times when the low-resistivity unfrozen silt layer extends to the base of the unfrozen  
397 gravels, which is a more resolvable target (Figure 8F).

398 A more detailed analysis of the changes in resistivity and ice-saturation as a function of  
399 time, and for the differences between hydrostatic and gaining lake conditions, is  
400 presented in Figure 9. Average values of resistivity/ice-saturation within 100 m of the  
401 lake center are shown within the gravel layer at a depth of 15 m (Figure 9A) and a depth  
402 of 50 m within the silt layer (Figure 9B) at 20 year time intervals. Outputs are displayed  
403 for both 6 m-deep hydrostatic and gaining lake scenarios. Thawing due to conduction  
404 occurs over the first ~200 years within the gravel layer (Figure 9A), with similar trends  
405 for both the hydrostatic and gaining lake conditions and no clear relationship to the talik  
406 formation times indicated as vertical lines. Conduction-dominated thaw is observed for  
407 the gravel layer in the gaining lake scenario because significant advection does not occur  
408 until after the thaw bulb has extended beneath the gravel layer. In the deeper silt layer  
409 (Figure 9B), however, very different trends are observed for the hydrostatic and gaining  
410 lake conditions. Ice content decreases gradually as thawing occurs in the hydrostatic  
411 scenario, consistent with conduction-dominated thaw, reaching a minimum near the time  
412 of talik formation at 687 years (Wellman et al., 2013, Table 3). In contrast, there is a  
413 rapid loss in ice content in the gaining lake scenario resulting from the influence of  
414 advective heat transport as groundwater is able to move upwards through the evolving  
415 talik beneath the lake. This rapid loss in ice content begins after the gravel layer thaws,  
416 and reaches a minimum near the 258-year time of talik formation for this scenario. These  
417 trends, captured by the AEM-derived resistivity models, are consistent with the plots of  
418 change in ice volume output from the SUTRA simulations reported by Wellman et al.  
419 (2013, Figure 3).

### 420 **3.3 Near-Surface Resolution**

421 Finally, we focus on the upper sand layer (Unit 1), which is generally too thin (2 m) and  
422 resistive ( $> 600$  ohm-m) to be resolved using AEM data; though may be imaged using  
423 other ground-based electrical or electromagnetic geophysical methods. Seasonal thaw  
424 and surface runoff causes locally reduced resistivity values in the upper 1 m, which is still  
425 too shallow to resolve adequately using AEM data. In practice, shallow thaw and  
426 sporadic permafrost trends are observed to greater depths in many locations, including

427 inactive or abandoned channels (Jepsen et al., 2013b). To simulate these types of  
428 features, the shallow resistivity structure of the 6 m-deep hydrostatic lake scenario at  
429 1,000 years is manually modified to include three synthetic ‘channels’. These channels  
430 are not intended to represent realistic pathways relative to the lake and the hydrologic  
431 simulations; they are solely for the purpose of illustrating the ability to resolve shallow  
432 resistivity features.

433 Figure 10A shows the three channels in a zoomed-in view of the uppermost portion of the  
434 model outside the lake extent. Each channel is 100 m wide, but with different depths: 1  
435 m (half the Unit 1 thickness), 2 m (full Unit 1 thickness) and 3 m (extending into the top  
436 of Unit 2). Analysis of AEM data simulated for this model, presented as the McMC  
437 average model, are shown in Figure 10B. All three channels are clearly identified, but  
438 their thicknesses and resistivity values are overestimated and cannot be distinguished  
439 from one another. To explore the possibility of better resolving these shallow features,  
440 synthetic EM data are simulated using the characteristics of a ground-based multi-  
441 frequency EM tool (the GEM-2 instrument) that can be hand carried or towed behind a  
442 vehicle, and is commonly used for shallow investigations. The McMC average model  
443 result for the simulated shallow EM data is shown in Figure 10C. An error model with  
444 4% relative data errors and an absolute error floor of 75 ppm was used for the GEM-2  
445 data. Channel thicknesses and resistivity values are better resolved compared with the  
446 AEM result, though the 1 m-deep channel near  $r = 800$  m appears both too thick and too  
447 resistive. In addition, the shallow EM data show some sensitivity to the interface at 2-m  
448 depth between frozen silty sands and frozen gravels, though the depth of this interface is  
449 over-estimated due to the limited sensitivity to these very resistive features.

#### 450 **4 Discussion**

451 Understanding the hydrogeophysical responses to permafrost dynamics under different  
452 hydrologic and climatic conditions, and in different geological settings, is important for  
453 guiding the interpretation of existing geophysical datasets and also for planning future  
454 surveys. Geophysical models are inherently uncertain and ambiguous because of (1) the  
455 resolution limitations of any geophysical method and (2) the weak or non-unique  
456 relationship between hydrologic properties and geophysical properties. We have  
457 presented a general framework for coupling airborne and ground-based electromagnetic

458 predictions to hydrologic simulations of permafrost evolution, including a novel physical  
459 property relationship that accounts for the electrical response to changes in lithology,  
460 temperature, and ice content, as well as a rigorous analysis of geophysical parameter  
461 uncertainty. Although the focus here is on AEM data, other types of electrical or  
462 electromagnetic measurements could be readily simulated using the same resistivity  
463 model. Future efforts will focus on the simulation of other types of geophysical data (e.g.  
464 nuclear magnetic resonance or ground penetrating radar) using the same basic modeling  
465 approach.

466 In the specific examples of lake talik evolution presented here, which are modeled after  
467 the physical setting of the Yukon Flats, Alaska (Minsley et al., 2012b), AEM data are  
468 shown to be generally capable of resolving large-scale permafrost and geological features  
469 (Figure 5), as well as thermally and hydrologically induced changes in permafrost (Figure  
470 8, Figure 9). The Bayesian MCMC analysis provides useful details about model  
471 resolution and uncertainty that cannot be assessed using traditional inversion methods  
472 that produce a single ‘best’ model. A fortuitous aspect of the Yukon Flats model is the  
473 fact that the silt layer (Unit 3) is relatively conductive compared with the overlying  
474 gravels (Unit 2), making it a good target for electromagnetic methods. If the order of  
475 these layers were reversed, if the base of permafrost were hosted in a relatively resistive  
476 lithology, or if the base of permafrost was significantly deeper, AEM data would not  
477 likely resolve the overall structure with such good fidelity. In addition, knowledge of the  
478 stratigraphy helps to remove the ambiguity between unfrozen gravels and frozen silts,  
479 which have similar intermediate resistivity values (Figure 4, Figure 5). The methods  
480 developed here that use a physical property model to link hydrologic and geophysical  
481 properties provide the necessary framework to test other more challenging  
482 hydrogeological scenarios.

483 Two key challenges for the lake talik scenarios were identified: (1) resolving the details  
484 of partial ice saturation beneath the lake during talik formation, and (2) resolving near-  
485 surface details associated with shallow thaw. The first challenge is confirmed by Figure  
486 5 and Figure 8, which show that AEM data cannot resolve the details of partial ice  
487 saturation beneath a forming talik. However, there is clearly a change in the overall  
488 characteristics of the sub-lake resistivity structure as thaw increases (Figure 9). One

489 notable feature is the steadily decreasing depth to the top of the low-resistivity unfrozen  
490 silt (red) beneath the lake (Figure 5A-B) as thaw increases, ultimately terminating at the  
491 depth of the gravel-silt interface when fully unfrozen conditions exist (Figure 5C).  
492 Measurements of the difference in elevation between the interpreted top of unfrozen silt  
493 and the base of nearby frozen gravels were used by Jepsen et al. (2013a) to classify  
494 whether or not fully thawed conditions existed beneath lakes in the Yukon Flats AEM  
495 survey described by Minsley et al. (2012a). The simulations presented here support use  
496 of this metric to distinguish full versus partial thaw beneath lakes. However, without the  
497 presence of a lithological boundary, the shallowing base of permafrost associated with  
498 talik development beneath lakes would be much more difficult to distinguish. Finally, it  
499 is important to note that resistivity is sensitive primarily to unfrozen water content, and  
500 that significant unfrozen water can remain in relatively warm permafrost that is near 0 C,  
501 particularly in fine-grained sediments. Resistivity-derived estimates of talik boundaries  
502 defined by water content may therefore differ from the thermal boundary defined at 0 C.

503 The second challenge, to resolve near-surface details associated with supra-permafrost  
504 thaw, is addressed in Figure 10. For the scenarios considered here, AEM data can  
505 identify shallow thaw features, but have difficulty in discriminating their specific details.  
506 There are many combinations of resistivity and thickness that produce the same EM  
507 response; therefore, without additional information it is not possible to uniquely  
508 characterize both thaw depth and resistivity. Ground-based EM data show improved  
509 sensitivity to the shallow channels, and also limited sensitivity to the interface between  
510 resistive frozen gravels and frozen silty sands (Figure 5). By restricting the possible  
511 values of resistivity and/or thickness for one or more layers based on prior assumptions,  
512 Dafflon et al. (2013) showed that improved estimates of active layer and permafrost  
513 properties can be obtained. The quality of these estimates, of course, depends on the  
514 accuracy of prior constraints used. In many instances, it may be possible to auger into  
515 this shallow layer to provide direct observations that can be used as constraints. This  
516 approach could be readily applied to the ensemble of MCMC models. For example, if the  
517 resistivity of the channels in Figure 10A were known, the thickness of the channels could  
518 be estimated more accurately by selecting only the set of MCMC models with channel

519 resistivity close to the true value, thereby removing some of the ambiguity due to  
520 equivalences between layer resistivity and thickness.

521 AEM data are most likely to be useful for baseline characterization of subsurface  
522 properties as opposed to monitoring changes in permafrost. Although there are some  
523 cases of rapid change associated with near-surface freeze/thaw processes (Koch et al.,  
524 2013) or in the case of catastrophic loss of ice in the gaining lake scenario (Figure 9B)  
525 that may be of interest, large-scale changes in permafrost generally occur over much  
526 longer time periods than is practical for repeat AEM surveys. One exception could be  
527 related to infrastructure projects such as water reservoirs or mine tailing impoundments  
528 behind dams, where AEM could be useful for baseline characterization and repeat  
529 monitoring of the impact caused by human-induced permafrost change. Geophysical  
530 modeling, thermophysical hydrologic modeling, and field observations create a synergy  
531 that provides greater insight than any individual approach, and can be useful for future  
532 characterization of coupled permafrost and hydrologic processes.

## 533 **5 Summary**

534 Analysis of AEM surveys provide a means for remotely detecting subsurface electrical  
535 resistivity associated with the co-evolution of permafrost and hydrologic systems over  
536 areas relevant to catchment-scale and larger processes. Coupled hydrogeophysical  
537 simulations using a novel physical property relationship that accounts for the effects of  
538 lithology, ice saturation, and temperature on electrical resistivity provide a systematic  
539 framework for exploring the geophysical response to various scenarios of permafrost  
540 evolution under different hydrological forcing. This modeling approach provides a  
541 means of robustly testing the interpretation of AEM data given the paucity of deep  
542 boreholes and other ground truth data that are needed to characterize subsurface  
543 permafrost. A robust uncertainty analysis of the geophysical simulations provides  
544 important new quantitative information about the types of features that can be resolved  
545 using AEM data given the inherent resolution limitations of geophysical measurements  
546 and ambiguities in the physical property relationships. In the scenarios considered here,  
547 we have shown that large-scale geologic and permafrost structure is accurately estimated.  
548 Sublacustrine thaw can also be identified, but the specific geometry of partial ice

549 saturation beneath lakes can be poorly resolved by AEM data. Understanding the  
550 geophysical response to known simulations is helpful both for guiding the interpretation  
551 of existing AEM data, and also to plan future surveys and other ground-based data  
552 acquisition efforts.

### 553 **Author contribution**

554 B. M. carried out the geophysical forward and inverse simulations, and prepared the  
555 manuscript with contributions from all co-authors. T. W. and M. W. provided SUTRA  
556 simulation results and hydrologic modeling expertise. A. R. helped to establish the  
557 petrophysical relationships used to define the electrical resistivity model used in this  
558 study.

### 559 **Acknowledgements**

560 This work was supported by the Strategic Environmental Research and  
561 Development Program (SERDP), through grant #RC-2111. We gratefully  
562 acknowledge additional support from the USGS National Research Program and the  
563 USGS Geophysical Methods Development Project. USGS reviews provided by Josh  
564 Koch and Marty Briggs have greatly improved this manuscript.

565

566 **References**

- 567 Anthony, K. M. W., Anthony, P., Grosse, G. and Chanton, J.: Geologic methane seeps  
568 along boundaries of Arctic permafrost thaw and melting glaciers, *Nat. Geosci.*, 5,  
569 419–426, doi:10.1038/ngeo1480, 2012.
- 570 Archie, G. E.: The electrical resistivity log as an aid in determining some reservoir  
571 characteristics, *Trans Amer Inst Min. Metall. Pet. Eng.*, 146, 54–62, 1942.
- 572 Aster, R. C., Borchers, B. and Thurber, C. H.: *Parameter Estimation and Inverse*  
573 *Problems*, Elsevier, Amsterdam., 2005.
- 574 Ball, L. B., Smith, B. D., Minsley, B. J., Abraham, J. D., Voss, C. I., Deszcz-Pan, M. and  
575 Cannia, J. C.: Airborne electromagnetic and magnetic survey data of the Yukon Flats  
576 and Ft. Wainwright areas, central Alaska, June 2010, U.S. Geological Survey Open-  
577 File Report 2011-1304., 2011.
- 578 Beamish, D.: Airborne EM footprints, *Geophys. Prospect.*, 51(1), 49–60,  
579 doi:10.1046/j.1365-2478.2003.00353.x, 2003.
- 580 Bense, V. F., Ferguson, G. and Kooi, H.: Evolution of shallow groundwater flow  
581 systems in areas of degrading permafrost, *Geophys. Res. Lett.*, 36, L22401,  
582 doi:200910.1029/2009GL039225, 2009.
- 583 Briggs, M. A., Walvoord, M. A., McKenzie, J. M., Voss, C. I., Day-Lewis, F. D. and Lane, J.  
584 W.: New permafrost is forming around shrinking Arctic lakes, but will it last?,  
585 *Geophys. Res. Lett.*, 41(5), 2014GL059251, doi:10.1002/2014GL059251, 2014.
- 586 Callegary, J. B., Kikuchi, C. P., Koch, J. C., Lilly, M. R. and Leake, S. A.: Review:  
587 Groundwater in Alaska (USA), *Hydrogeol. J.*, 21(1), 25–39, doi:10.1007/s10040-012-  
588 0940-5, 2013.
- 589 Dafflon, B., Hubbard, S. S., Ulrich, C. and Peterson, J. E.: Electrical Conductivity  
590 Imaging of Active Layer and Permafrost in an Arctic Ecosystem, through Advanced  
591 Inversion of Electromagnetic Induction Data, *Vadose Zone J.*, 12(4), vzj2012.0161,  
592 doi:10.2136/vzj2012.0161, 2013.
- 593 Day-Lewis, F. D., Singha, K. and Binley, A. M.: Applying petrophysical models to radar  
594 travel time and electrical resistivity tomograms: Resolution-dependent limitations,  
595 *J. Geophys. Res. Solid Earth*, 110, B08206, doi:10.1029/2004JB003569, 2005.
- 596 Farquharson, C. G., Oldenburg, D. W. and Routh, P. S.: Simultaneous 1D inversion of  
597 loop–loop electromagnetic data for magnetic susceptibility and electrical  
598 conductivity, *Geophysics*, 68(6), 1857–1869, doi:10.1190/1.1635038, 2003.
- 599 Green, P. J.: Reversible jump Markov chain Monte Carlo computation and Bayesian  
600 model determination, *Biometrika*, 82(4), 711–732, 1995.

- 601 Hastings, W. K.: Monte Carlo sampling methods using Markov chains and their  
602 applications, *Biometrika*, 57(1), 97–109, doi:10.1093/biomet/57.1.97, 1970.
- 603 Hauck, C., Böttcher, M. and Maurer, H.: A new model for estimating subsurface ice  
604 content based on combined electrical and seismic data sets, *The Cryosphere*, 5(2),  
605 453–468, doi:10.5194/tc-5-453-2011, 2011.
- 606 Hinzman, L. D., Bettez, N. D., Bolton, W. R., Chapin, F. S., Dyurgerov, M. B., Fastie, C. L.,  
607 Griffith, B., Hollister, R. D., Hope, A., Huntington, H. P., Jensen, A. M., Jia, G. J.,  
608 Jorgenson, T., Kane, D. L., Klein, D. R., Kofinas, G., Lynch, A. H., Lloyd, A. H., McGuire,  
609 A. D., Nelson, F. E., Oechel, W. C., Osterkamp, T. E., Racine, C. H., Romanovsky, V. E.,  
610 Stone, R. S., Stow, D. A., Sturm, M., Tweedie, C. E., Vourlitis, G. L., Walker, M. D.,  
611 Walker, D. A., Webber, P. J., Welker, J. M., Winker, K. S. and Yoshikawa, K.: Evidence  
612 and implications of recent climate change in northern Alaska and other Arctic  
613 regions, *Clim. Change*, 72(3), 251–298, doi:10.1007/s10584-005-5352-2, 2005.
- 614 Hoekstra, P., Sellmann, P. V. and Delaney, A.: Ground and airborne resistivity surveys  
615 of permafrost near Fairbanks, Alaska, *Geophysics*, 40(4), 641–656, 1975.
- 616 Huang, H. P. and Won, I. J.: Real-time resistivity sounding using a hand-held  
617 broadband electromagnetic sensor, *Geophysics*, 68(4), 1224–1231, 2003.
- 618 Hubbard, S. S., Gangodagamage, C., Dafflon, B., Wainwright, H., Peterson, J.,  
619 Gusmeroli, A., Ulrich, C., Wu, Y., Wilson, C., Rowland, J., Tweedie, C. and Wullschleger,  
620 S. D.: Quantifying and relating land-surface and subsurface variability in permafrost  
621 environments using LiDAR and surface geophysical datasets, *Hydrogeol. J.*, 21(1),  
622 149–169, doi:10.1007/s10040-012-0939-y, 2013.
- 623 Jepsen, S. M., Voss, C. I., Walvoord, M. A., Minsley, B. J. and Rover, J.: Linkages  
624 between lake shrinkage/expansion and sublacustrine permafrost distribution  
625 determined from remote sensing of interior Alaska, USA, *Geophys. Res. Lett.*, 40(5),  
626 882–887, doi:10.1002/grl.50187, 2013a.
- 627 Jepsen, S. M., Voss, C. I., Walvoord, M. A., Rose, J. R., Minsley, B. J. and Smith, B. D.:  
628 Sensitivity analysis of lake mass balance in discontinuous permafrost: the example  
629 of disappearing Twelvemile Lake, Yukon Flats, Alaska (USA), *Hydrogeol. J.*, 21(1),  
630 185–200, doi:10.1007/s10040-012-0896-5, 2013b.
- 631 Jorgenson, M. T., Racine, C., Walters, J. and Osterkamp, T.: Permafrost degradation  
632 and ecological changes associated with a warming climate in central Alaska, *Clim.*  
633 *Change*, 48(4), 551–579, 2001.
- 634 Keller, G. V. and Frischknecht, F. C.: *Electrical methods in geophysical prospecting*,  
635 Pergamon Press, Oxford., 1966.
- 636 Koch, J. C., Ewing, S. A., Striegl, R. and McKnight, D. M.: Rapid runoff via shallow  
637 throughflow and deeper preferential flow in a boreal catchment underlain by frozen

638 silt (Alaska, USA), *Hydrogeol. J.*, 21(1), 93–106, doi:10.1007/s10040-012-0934-3,  
639 2013.

640 Koven, C. D., Ringeval, B., Friedlingstein, P., Ciais, P., Cadule, P., Khvorostyanov, D.,  
641 Krinner, G. and Tarnocai, C.: Permafrost carbon-climate feedbacks accelerate global  
642 warming, *Proc. Natl. Acad. Sci.*, 108(36), 14769–14774,  
643 doi:10.1073/pnas.1103910108, 2011.

644 Larsen, P. H., Goldsmith, S., Smith, O., Wilson, M. L., Strzepek, K., Chinowsky, P. and  
645 Saylor, B.: Estimating future costs for Alaska public infrastructure at risk from  
646 climate change, *Glob. Environ. Gov. Another World Possible*, 18(3), 442–457,  
647 doi:10.1016/j.gloenvcha.2008.03.005, 2008.

648 Liu, L., Schaefer, K., Zhang, T. and Wahr, J.: Estimating 1992–2000 average active  
649 layer thickness on the Alaskan North Slope from remotely sensed surface  
650 subsidence, *J. Geophys. Res. Earth Surf.*, 117, F01005, doi:10.1029/2011JF002041,  
651 2012.

652 Marion, G. M.: *Freeze-thaw processes and soil chemistry.*, 1995.

653 McKenzie, J. and Voss, C.: Permafrost thaw in a nested groundwater-flow system,  
654 *Hydrogeol. J.*, 21(1), 299–316, doi:10.1007/s10040-012-0942-3, 2013.

655 Metropolis, N., Rosenbluth, A., Rosenbluth, M., Teller, A. and Teller, E.: Equation of  
656 State Calculations by Fast Computing Machines, *J. Chem. Phys.*, 21(6), 1087–1092,  
657 doi:10.1063/1.1699114, 1953.

658 Minsley, B. J.: A trans-dimensional Bayesian Markov chain Monte Carlo algorithm for  
659 model assessment using frequency-domain electromagnetic data, *Geophys. J. Int.*,  
660 187(1), 252–272, doi:10.1111/j.1365-246X.2011.05165.x, 2011.

661 Minsley, B. J., Abraham, J. D., Smith, B. D., Cannia, J. C., Voss, C. I., Jorgenson, M. T.,  
662 Walvoord, M. A., Wylie, B. K., Anderson, L., Ball, L. B., Deszcz-Pan, M., Wellman, T. P.  
663 and Ager, T. A.: Airborne electromagnetic imaging of discontinuous permafrost,  
664 *Geophys. Res. Lett.*, 39, L02503, doi:10.1029/2011GL050079, 2012a.

665 Minsley, B. J., Abraham, J. D., Smith, B. D., Cannia, J. C., Voss, C. I., Jorgenson, M. T.,  
666 Walvoord, M. A., Wylie, B. K., Anderson, L., Ball, L. B., Deszcz-Pan, M., Wellman, T. P.  
667 and Ager, T. A.: Airborne electromagnetic imaging of discontinuous permafrost,  
668 *Geophys. Res. Lett.*, 39, L02503, doi:10.1029/2011GL050079, 2012b.

669 Minsley, B. J., Ajo-Franklin, J., Mukhopadhyay, A. and Morgan, F. D.:  
670 *Hydrogeophysical Methods for Analyzing Aquifer Storage and Recovery Systems*,  
671 *Ground Water*, 49(2), 250–269, 2011.

- 672 Nelson, F. E., Anisimov, O. A. and Shiklomanov, N. I.: Climate change and hazard  
673 zonation in the circum-Arctic permafrost regions, *Nat. Hazards*, 26(3), 203–225,  
674 2002.
- 675 O'Donnell, J. A., Aiken, G. R., Walvoord, M. A. and Butler, K. D.: Dissolved organic  
676 matter composition of winter flow in the Yukon River basin: Implications of  
677 permafrost thaw and increased groundwater discharge, *Glob. Biogeochem. Cycles*,  
678 26(4), GB0E06, doi:10.1029/2012GB004341, 2012.
- 679 O'Donnell, J. A., Harden, J. W., McGuire, A. D., Kanevskiy, M. Z., Jorgenson, M. T. and  
680 Xu, X.: The effect of fire and permafrost interactions on soil carbon accumulation in  
681 an upland black spruce ecosystem of interior Alaska: implications for post-thaw  
682 carbon loss, *Glob. Change Biol.*, 17(3), 1461–1474, doi:10.1111/j.1365-  
683 2486.2010.02358.x, 2011.
- 684 Oldenborger, G. A. and Routh, P. S.: The point-spread function measure of resolution  
685 for the 3-D electrical resistivity experiment, *Geophys. J. Int.*, 176(2), 405–414, 2009.
- 686 Palacky, G. J.: Resistivity characteristics of geologic targets, in *Electromagnetic*  
687 *methods in applied geophysics: Volume 1, theory*, edited by M. N. Nabighian, pp. 53–  
688 129, Society of Exploration Geophysicists, Tulsa., 1987.
- 689 Panda, S. K., Prakash, A., Solie, D. N., Romanovsky, V. E. and Jorgenson, M. T.: Remote  
690 sensing and field-based mapping of permafrost distribution along the Alaska  
691 Highway corridor, interior Alaska, *Permafr. Periglac. Process.*, 21(3), 271–281,  
692 doi:10.1002/ppp.686, 2010.
- 693 Parsekian, A. D., Grosse, G., Walbrecker, J. O., Müller-Petke, M., Keating, K., Liu, L.,  
694 Jones, B. M. and Knight, R.: Detecting unfrozen sediments below thermokarst lakes  
695 with surface nuclear magnetic resonance, *Geophys. Res. Lett.*, 40(3), 535–540,  
696 doi:10.1002/grl.50137, 2013.
- 697 Pastick, N. J., Jorgenson, M. T., Wylie, B. K., Rose, J. R., Rigge, M. and Walvoord, M. A.:  
698 Spatial variability and landscape controls of near-surface permafrost within the  
699 Alaskan Yukon River Basin, *J. Geophys. Res. Biogeosciences*, 119(6), 2013JG002594,  
700 doi:10.1002/2013JG002594, 2014.
- 701 Petrone, K. C., Hinzman, L. D., Jones, J., Shibata, H. and Boone, R.: The influence of fire  
702 and permafrost on sub-arctic stream chemistry during storms, *Hydrol. Process.*,  
703 21(4), 423–434, doi:10.1002/hyp.6247, 2007.
- 704 Revil, A.: Spectral induced polarization of shaly sands: Influence of the electrical  
705 double layer, *Water Resour. Res.*, 48(W02517), doi:10.1029/2011WR011260, 2012.
- 706 Revil, A., Cathles, L. M., Losh, S. and Nunn, J. A.: Electrical conductivity in shaly sands  
707 with geophysical applications, *J. Geophys. Res. Solid Earth*, 103(B10), 23925–23936,  
708 doi:10.1029/98JB02125, 1998.

- 709 Rinaldi, A. P., Todesco, M., Vandemeulebrouck, J., Revil, A. and Bonafede, M.:  
710 Electrical conductivity, ground displacement, gravity changes, and gas flow at  
711 Solfatara crater (Campi Flegrei caldera, Italy): Results from numerical modeling, J.  
712 Volcanol. Geotherm. Res., 207(3–4), 93–105, doi:10.1016/j.jvolgeores.2011.07.008,  
713 2011.
- 714 Roach, J., Griffith, B., Verbyla, B. and Jones, J.: Mechanisms influencing changes in  
715 lake area in Alaskan boreal forest, Glob. Change Biol., 17, 2567–2583,  
716 doi:10.1111/j.1365-2486.2011.02446.x, 2011.
- 717 Rover, J., Ji, L., Wylie, B. K. and Tieszen, L. L.: Establishing water body areal extent  
718 trends in interior Alaska from multi-temporal Landsat data, Remote Sens. Lett., 3(7),  
719 595–604, doi:10.1080/01431161.2011.643507, 2012.
- 720 Rowland, J. C., Travis, B. J. and Wilson, C. J.: The role of advective heat transport in  
721 talik development beneath lakes and ponds in discontinuous permafrost, Geophys.  
722 Res. Lett., 38, L17504, doi:10.1029/2011GL048497, 2011.
- 723 Sambridge, M., Bodin, T., Gallagher, K. and Tkalčić, H.: Transdimensional inference in  
724 the geosciences, Philos. Trans. R. Soc. Math. Phys. Eng. Sci., 371(1984),  
725 doi:10.1098/rsta.2011.0547, 2013.
- 726 Sen, P. N. and Goode, P. A.: Influence of temperature on electrical conductivity on  
727 shaly sands, Geophysics, 57(1), 89–96, doi:10.1190/1.1443191, 1992.
- 728 Sen, P., Scala, C. and Cohen, M.: A self - similar model for sedimentary rocks with  
729 application to the dielectric constant of fused glass beads, Geophysics, 46(5), 781–  
730 795, doi:10.1190/1.1441215, 1981.
- 731 Siemon, B.: Electromagnetic methods - frequency domain, in Groundwater  
732 Geophysics: A Tool for Hydrogeology, edited by R. Kirsch, pp. 155–176, Springer-  
733 Verlag, Berlin., 2006.
- 734 Striegl, R. G., Aiken, G. R., Dornblaser, M. M., Raymond, P. A. and Wickland, K. P.: A  
735 decrease in discharge-normalized DOC export by the Yukon River during summer  
736 through autumn, Geophys. Res. Lett., 32, L21413, doi:10.1190/1.1443191, 2005.
- 737 Voss, C. I. and Provost, A. M.: SUTRA, A model for saturated-unsaturated, variable  
738 density ground-water flow with solute or energy transport, U.S. Geological Survey  
739 Water-Resources Investigations Report 02-4231., 2002.
- 740 Walvoord, M. A. and Striegl, R. G.: Increased groundwater to stream discharge from  
741 permafrost thawing in the Yukon River basin: Potential impacts on lateral export of  
742 carbon and nitrogen, Geophys. Res. Lett., 34, L12402,  
743 doi:200710.1029/2007GL030216, 2007.

- 744 Walvoord, M. A., Voss, C. I. and Wellman, T. P.: Influence of permafrost distribution  
745 on groundwater flow in the context of climate-driven permafrost thaw: Example  
746 from Yukon Flats Basin, Alaska, United States, *Water Resour. Res.*, 48(7), W07524,  
747 doi:10.1029/2011WR011595, 2012.
- 748 Ward, S. H. and Hohmann, G. W.: Electromagnetic theory for geophysical  
749 applications, in *Electromagnetic methods in applied geophysics: Volume 1, theory*,  
750 edited by M. N. Nabighian, pp. 131–311, Society of Exploration Geophysicists, Tulsa.,  
751 1988.
- 752 Wellman, T. P., Voss, C. I. and Walvoord, M. A.: Impacts of climate, lake size, and  
753 supra- and sub-permafrost groundwater flow on lake-talik evolution, Yukon Flats,  
754 Alaska (USA), *Hydrogeol. J.*, 21(1), 281–298, doi:10.1007/s10040-012-0941-4,  
755 2013.
- 756 Williams, J. R.: Geologic reconnaissance of the Yukon Flats District Alaska, U.S.  
757 Geological Survey Bulletin 1111-H, 1962.
- 758 Yoshikawa, K., Bolton, W. R., Romanovsky, V. E., Fukuda, M. and Hinzman, L. D.:  
759 Impacts of wildfire on the permafrost in the boreal forests of Interior Alaska, *J.*  
760 *Geophys. Res. Atmospheres*, 107(8148), doi:10.1029/2001JD000438, 2002.
- 761

762 **Tables**

763 Table 1. Description of geologic units and physical properties used in numerical  
 764 simulations. Entries separated by commas represent parameters with different values for  
 765 each of the lithologic units.

<i>Geologic unit properties</i>	
Lithology:	
Unit 1	Sediment (silty sand)
Unit 2	Sediment (gravelly sand)
Unit 3	Lacustrine silt
Unit depth range [m]	0-2, 2-30, 30-250
Porosity [-]	0.25, 0.25, 0.20
<i>Geophysical parameters</i>	
Archie cementation exponent ( $m$ ) [-]	1.5
Archie saturation exponent ( $n$ ) [-]	1.5
Water salinity ( $C$ ) [ppm]	250 ( $S_i = 0$ )
Na <sup>+</sup> ionic mobility ( $\beta$ ) [m <sup>2</sup> /Vs]	$5.8 \times 10^{-8}$ (25°C)
Cl <sup>-</sup> ionic mobility ( $\beta$ ) [m <sup>2</sup> /Vs]	$7.9 \times 10^{-8}$ (25°C)
Na <sup>+</sup> surface ionic mobility ( $\beta_s$ ) [m <sup>2</sup> /Vs]	$0.51 \times 10^{-8}$ (25°C)
Grain mass density ( $\rho_g$ ) [kg/m <sup>3</sup> ]	2650
Cation exchange capacity ( $\chi$ ) [C/kg]	200, 10, 500
Salinity exponent ( $a$ ) [-]	0.8

766

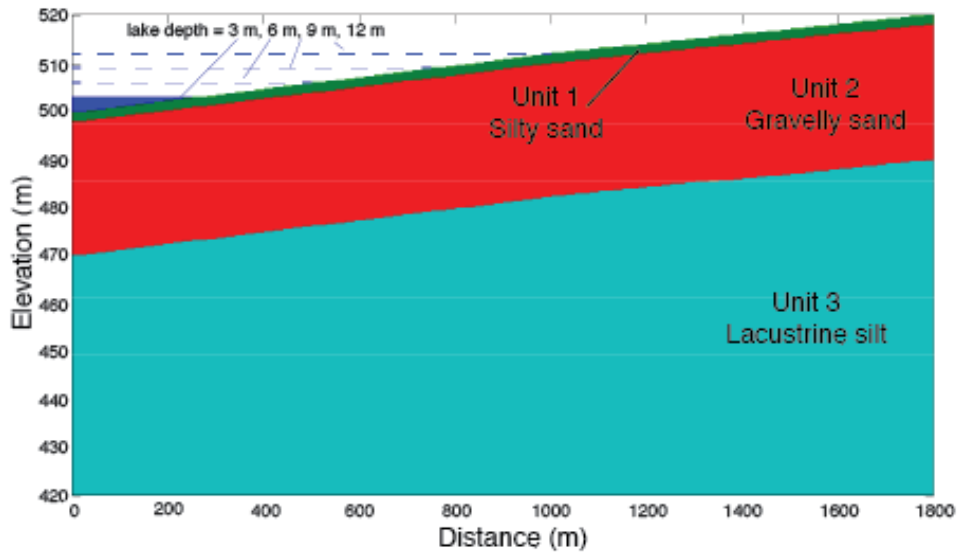
767

768 Table 2. Probability of ice saturation falling above or below specified thresholds based  
769 on the MCMC-derived resistivity probability distributions shown in Figure 7.

	<b>p(ice &lt; 0.5)</b>	<b>p(ice &gt; 0.95)</b>
<b>Unit 2 (gravel), <math>r = 0</math> m</b>	0.76	0.05
<b>Unit 2 (gravel), <math>r = 750</math> m</b>	0.00	0.88
<b>Unit 3 (silt), <math>r = 0</math> m</b>	0.76	0.05
<b>Unit 3 (silt), <math>r = 750</math> m</b>	0.00	0.98

770

771

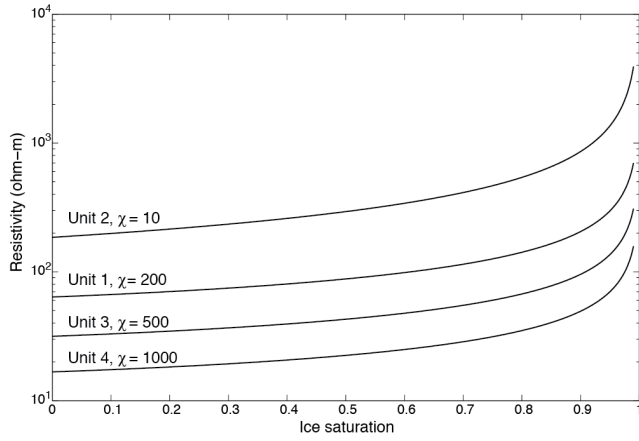


772

773 Figure 1. Axis-symmetric model geometry indicating different lithologic units and

774 simulated lake depths/extents.

775



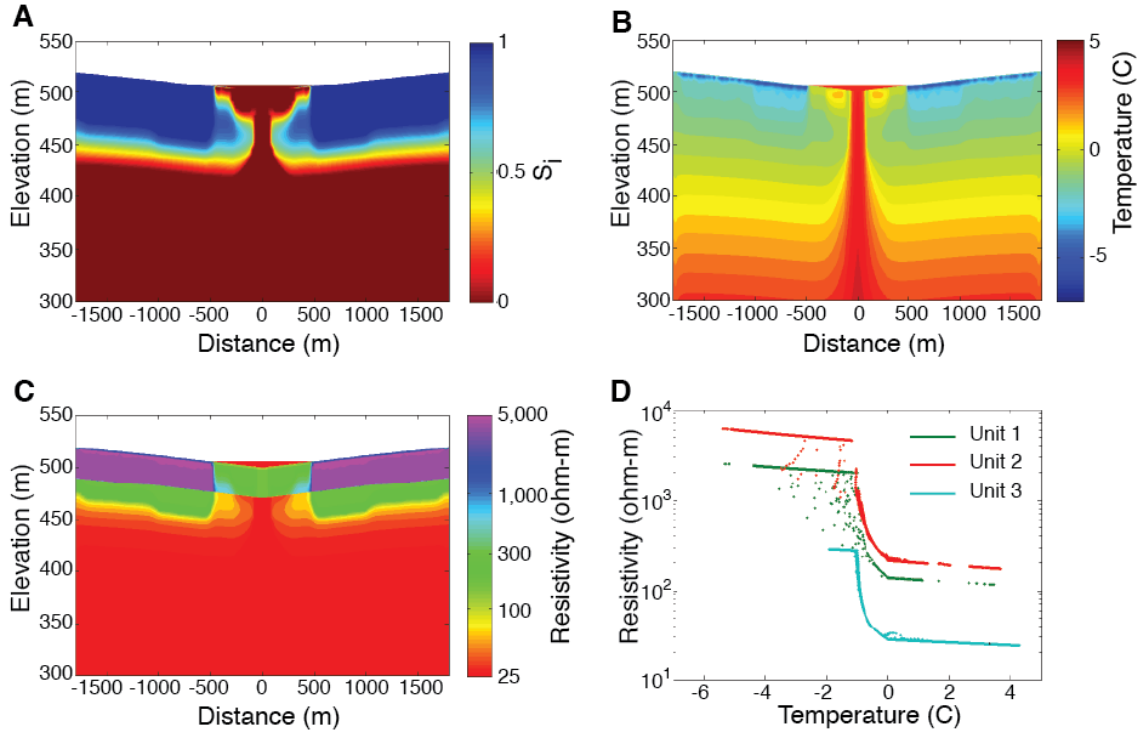
776

777 Figure 2. Bulk resistivity as a function of ice saturation using the physical properties  
 778 defined for each of the lithologic units described in Table 1.

779

780

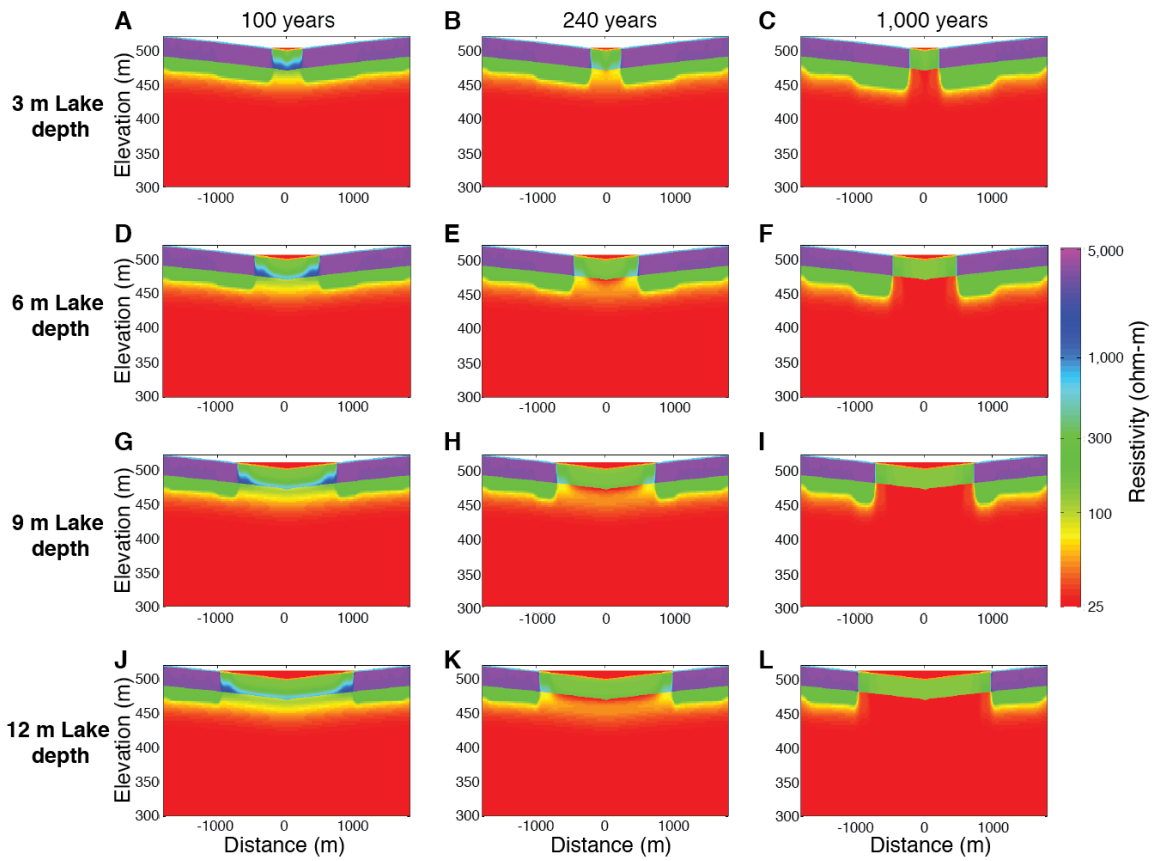
781



782

783 Figure 3. SUTRA model outputs and geophysical transformations from the 6-m gaining  
784 lake simulation at 240 years. Ice saturation (A) and temperature (B) are converted  
785 predictions of bulk resistivity (C). Variability in resistivity as a function of temperature  
786 is indicated in (D) for lithologic units 1-3.

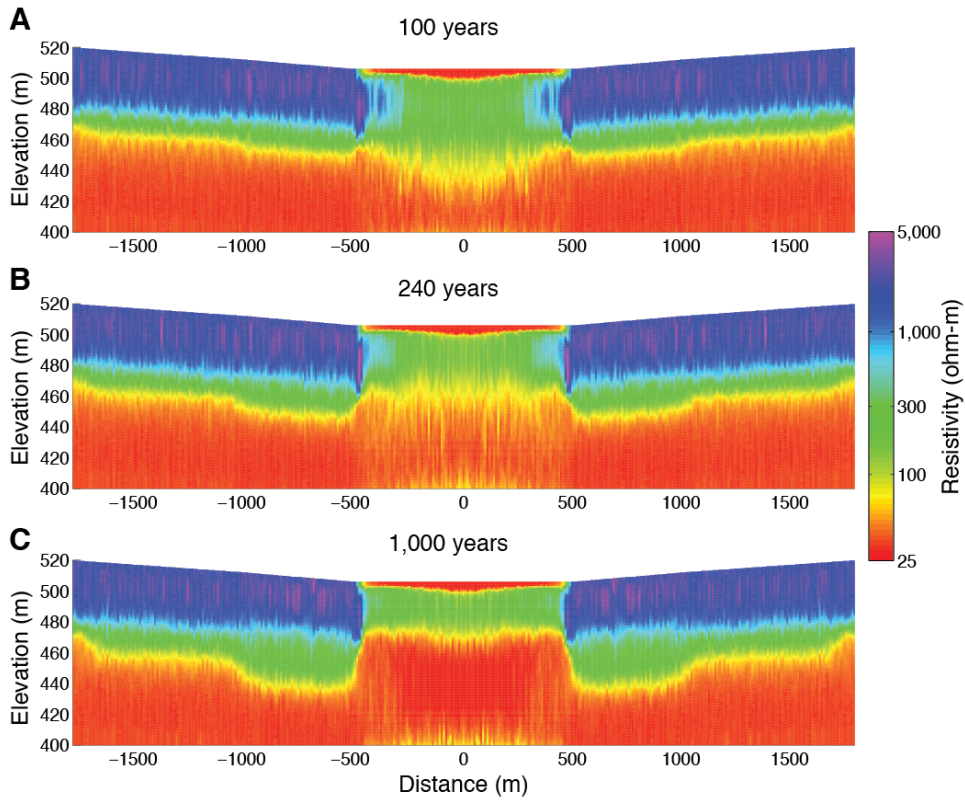
787



788

789 Figure 4. Synthetic bulk resistivity images under hydrostatic flow and current climate  
 790 conditions. Lake depths of 3 m (A-C), 6 m (D-F), 9 m (G-I), and 12 m (J-L) are  
 791 illustrated at simulation times 100, 240, and 1,000 years.

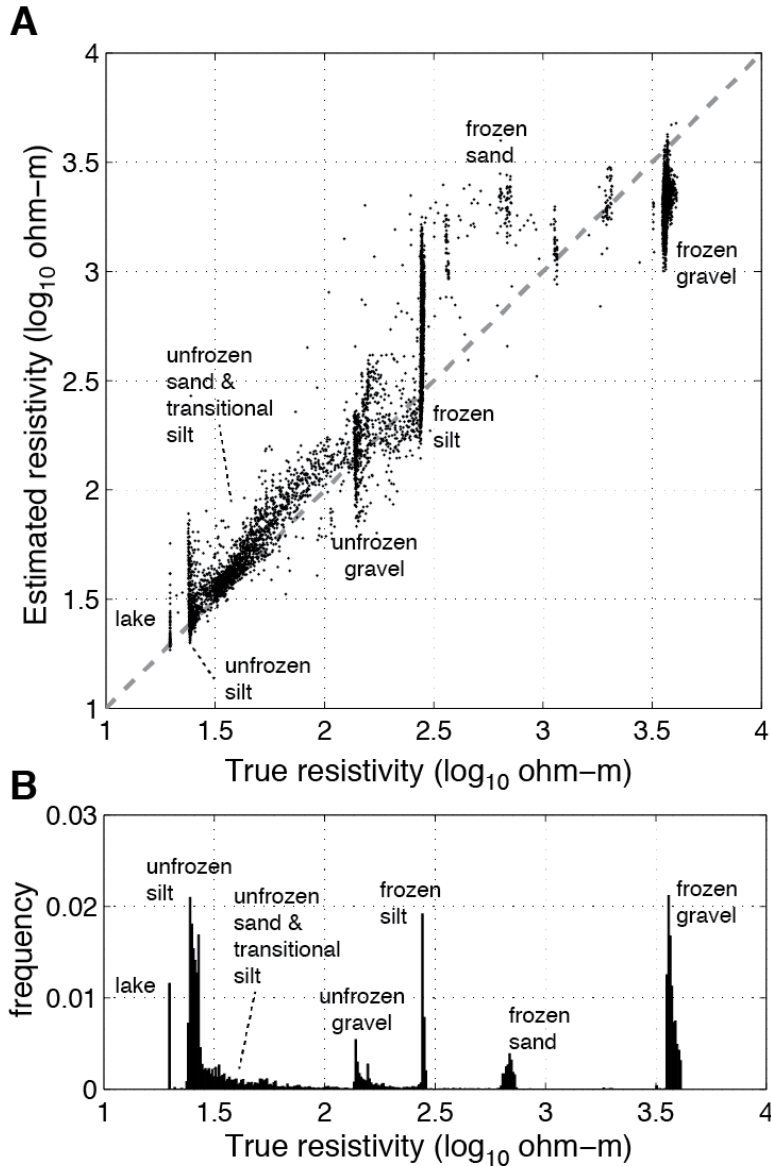
792



793

794 Figure 5. Mean resistivity model extracted from MCMC ensembles. Results are shown  
 795 for the 6-m-deep hydrostatic lake scenario outputs at (A) 100 years, (B) 240 years, and  
 796 (C) 1,000 years.

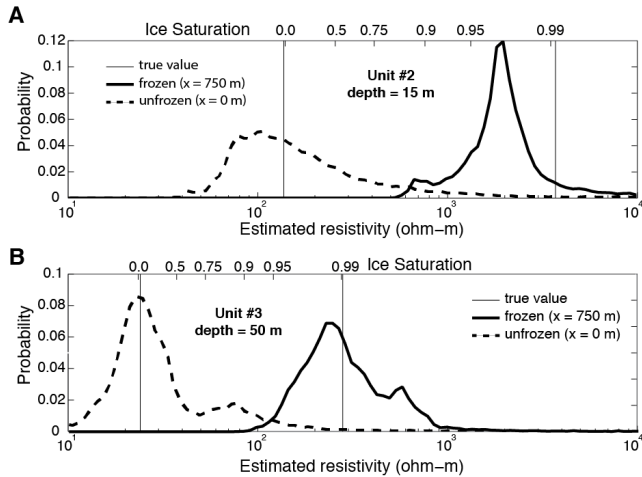
797



798

799 Figure 6. Performance of geophysical parameter estimation in recovering true parameter  
 800 values. (A) True versus MCMC-estimated resistivity values for the hydrostatic 6-m-deep  
 801 lake scenario at simulation time 1,000 years, compared with the frequency distribution of  
 802 true resistivity values (B). Estimated resistivity values generally fall along the dashed 1:1  
 803 line in (A), with exceptions being under-prediction of the resistive frozen gravels, over-  
 804 prediction of the thin surficial frozen sand, and some over-prediction of the frozen silt  
 805 where it is in contact with frozen gravel.

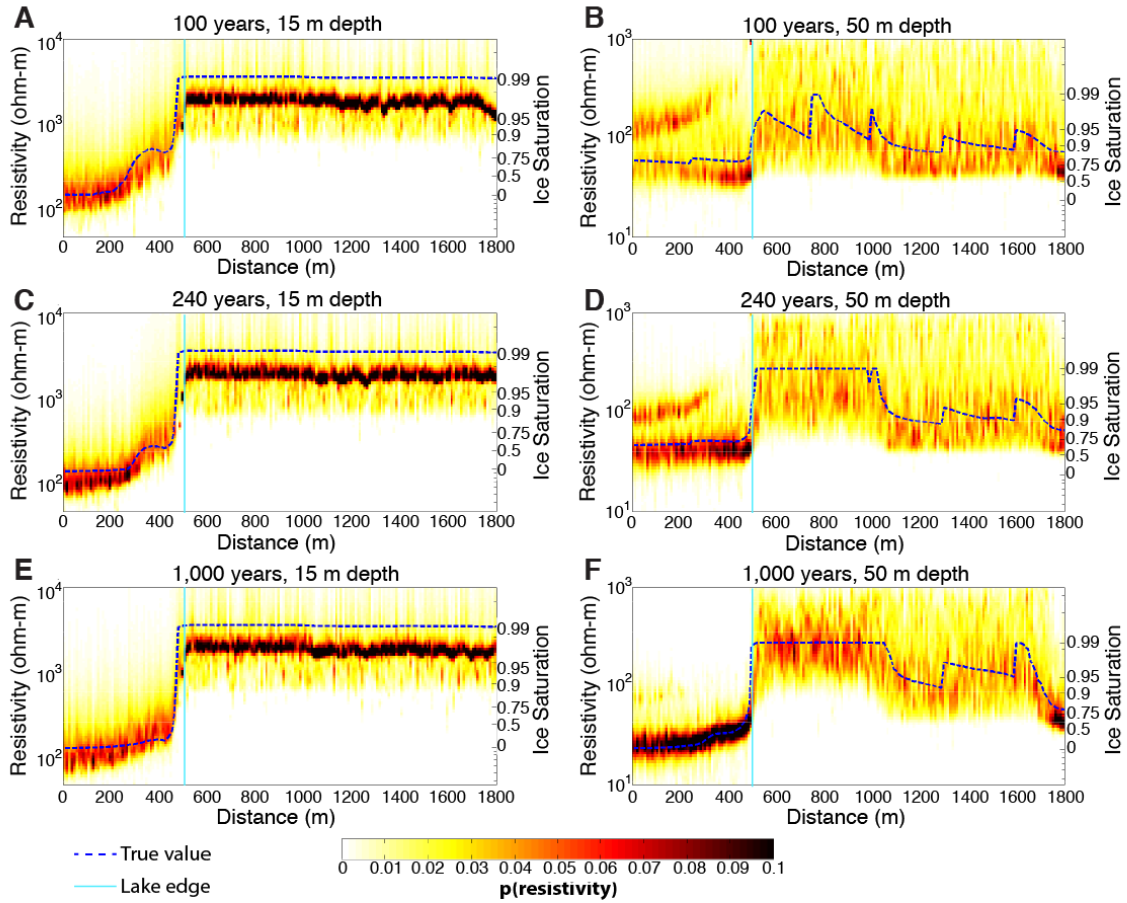
806



807

808 Figure 7. McMC-estimated resistivity posterior distributions within frozen and unfrozen  
 809 unit #2 gravels (A) and frozen and unfrozen unit #3 silts (B) for the hydrostatic 6-m-deep  
 810 lake scenario at 1,000 years. Unfrozen resistivity distributions are extracted beneath the  
 811 center of the lake ( $r = 0$ ) at depths of 15 m and 50 m for the gravels and silts,  
 812 respectively. Frozen distributions are extracted at the same depths, but at  $r = 750$  m. The  
 813 upper x-axes labels indicate approximate ice saturation based on the lithology-dependent  
 814 ice saturation versus resistivity curves shown in Figure 2.

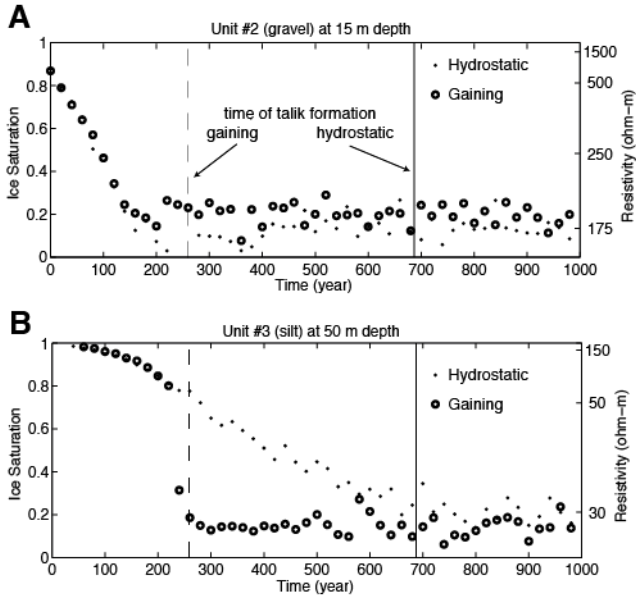
815



816

817 Figure 8. Resistivity probability distributions for the hydrostatic 6-m-deep lake scenario  
 818 at simulation times 100 years (A-B), 240 years (C-D), and 1,000 years (E-F). Shading in  
 819 each image represents the probability distribution at depths of 15 m (A, C, E) and 50 m  
 820 (B, D, F) from the lake center ( $r = 0$  m) to the edge of the model ( $r = 1800$  m). Dashed  
 821 lines indicate the true resistivity values. Ice saturation is displayed on the right axis of  
 822 each image, and is defined empirically for each lithology using the relationships in Figure  
 823 2.

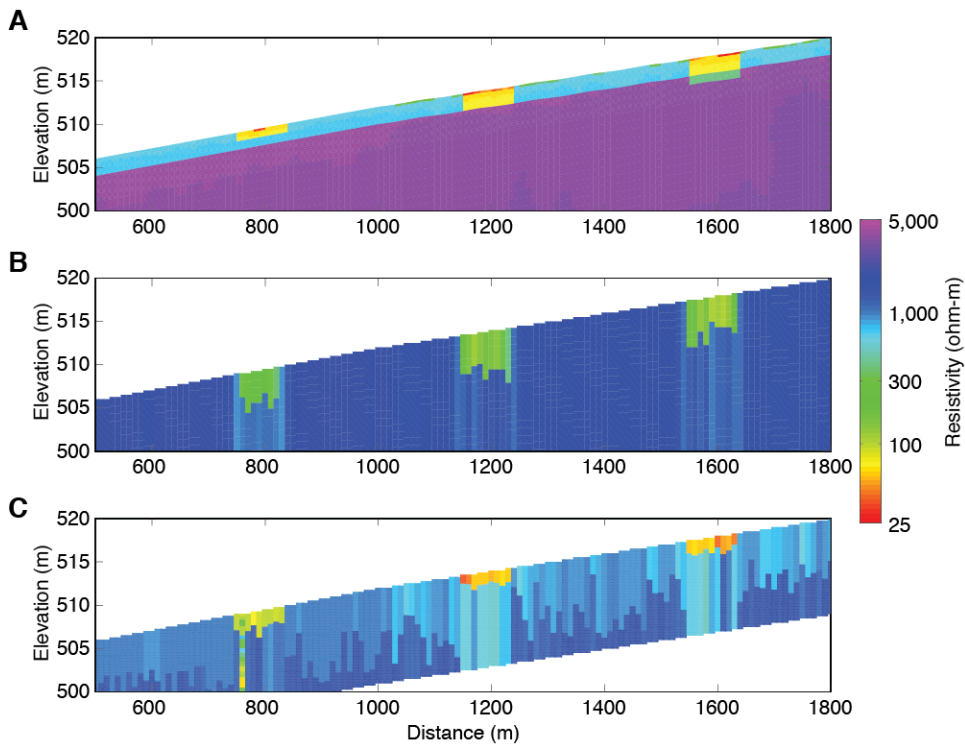
824



825

826 Figure 9. Change in ice saturation and resistivity as a function of time. Results are  
 827 shown for the 6-m-deep lake hydrostatic and gaining lake scenarios within (A) the gravel  
 828 layer, unit #2, at a depth of 15 m and (B) the silt layer, unit #3, at a depth of 50 m.

829



830

831 Figure 10. Comparison of airborne and ground-based measurements for recovering  
 832 shallow thaw features. (A) True shallow resistivity structure extracted from the  
 833 hydrostatic 6-m-deep lake scenario at a simulation time of 1,000 years, shown outside of  
 834 the lake extent (distance > 500 m). Three shallow low-resistivity channels with  
 835 thicknesses 1 m, 2 m, and 3 m were added to the resistivity model to provide added  
 836 contrast. MCMC-derived results using simulated AEM data (B) and ground-based EM  
 837 data (C) illustrate the capability of these systems to image shallow features.

838